High-Strength Chemical-Vapor–Deposited Graphene and Grain Boundaries

Gwan-Hyoung Lee,[1,2]* Ryan C. Cooper,[1]* Sung Joo An,[1] Sunwoo Lee,[3] Arend van der Zande,[1,4] Nicholas Petrone,[1] Alexandra G. Hammerberg,[1] Changgu Lee,[5,6] Bryan Crawford,[7] Warren Oliver,[7] Jeffrey W. Kysar,[1]† James Hone[1]†

Pristine graphene is the strongest material ever measured. However, large-area graphene films produced by means of chemical vapor deposition (CVD) are polycrystalline and thus contain grain boundaries that can potentially weaken the material. We combined structural characterization by means of transmission electron microscopy with nanoindentation in order to study the mechanical properties of CVD-graphene films with different grain sizes. We show that the elastic stiffness of CVD-graphene is identical to that of pristine graphene if postprocessing steps avoid damage or rippling. Its strength is only slightly reduced despite the existence of grain boundaries. Indentation tests directly on grain boundaries confirm that they are almost as strong as pristine. Graphene films consisting entirely of well-stitched grain boundaries can retain ultrahigh strength, which is critical for a large variety of applications, such as flexible electronics and strengthening components.

In bulk three-dimensional (3D) materials, the inevitable presence of bulk and surface defects limits the tensile strength to a value that typically falls well short of the intrinsic strength predicted for homogeneous tensile cleavage (*1*). Low-dimensional materials such as 2D graphene or quasi-1D carbon nanotubes can achieve record strength in part because of the lack of surface defects that often initiate fracture in 3D materials. However, using the ultrahigh strength of low-dimensional materials on the macroscale remains an open challenge, both from a technological perspective and as a matter of fundamental interest. At sufficiently large scales, all materials will contain lattice defects, and the effects of such defects should be magnified in low-dimensional materials because of a reduction in the number of dimensions in which a material can receive structural support: In the limit of a 1D atomic chain, even a single vacancy will reduce the tensile strength to zero. Moreover, the same lack of surface-bulk distinction that eliminates surface defects in low-dimensional materials also renders them extremely sensitive to damage during processing.

We have previously used nanoindentation of freely suspended films in an atomic force microscope (AFM) to show that graphene isolated through mechanical exfoliation is the strongest known material and, in its defect-free pristine state, can achieve its intrinsic strength before succumbing to rupture (*2*). However, graphene produced

---

[1] Department of Mechanical Engineering, Columbia University, New York, NY 10027, USA. [2] Samsung–Sungkyunkwan University (SKKU) Graphene Center (SSGC), Suwon 440-746, Korea. [3] Department of Electrical Engineering, Columbia University, New York, NY 10027, USA. [4] Energy Frontier Research Center, Columbia University, New York, NY 10027, USA. [5] School of Mechanical Engineering, SKKU, 2066, Seobu-ro, Jangan-gu, Suwon, Gyeonggi 440-746, Korea. [6] SKKU Advanced Institute of Nanotechnology (SAINT), SKKU, 2066, Seobu-ro, Jangan-gu, Suwon, Gyeonggi 440-746, Korea. [7] Nanomechanics, Oak Ridge, TN 37830, USA.

*These authors contributed equally to this work.
†Corresponding author. E-mail: jh2228@columbia.edu (J.H.); jk2079@columbia.edu (J.W.K.)

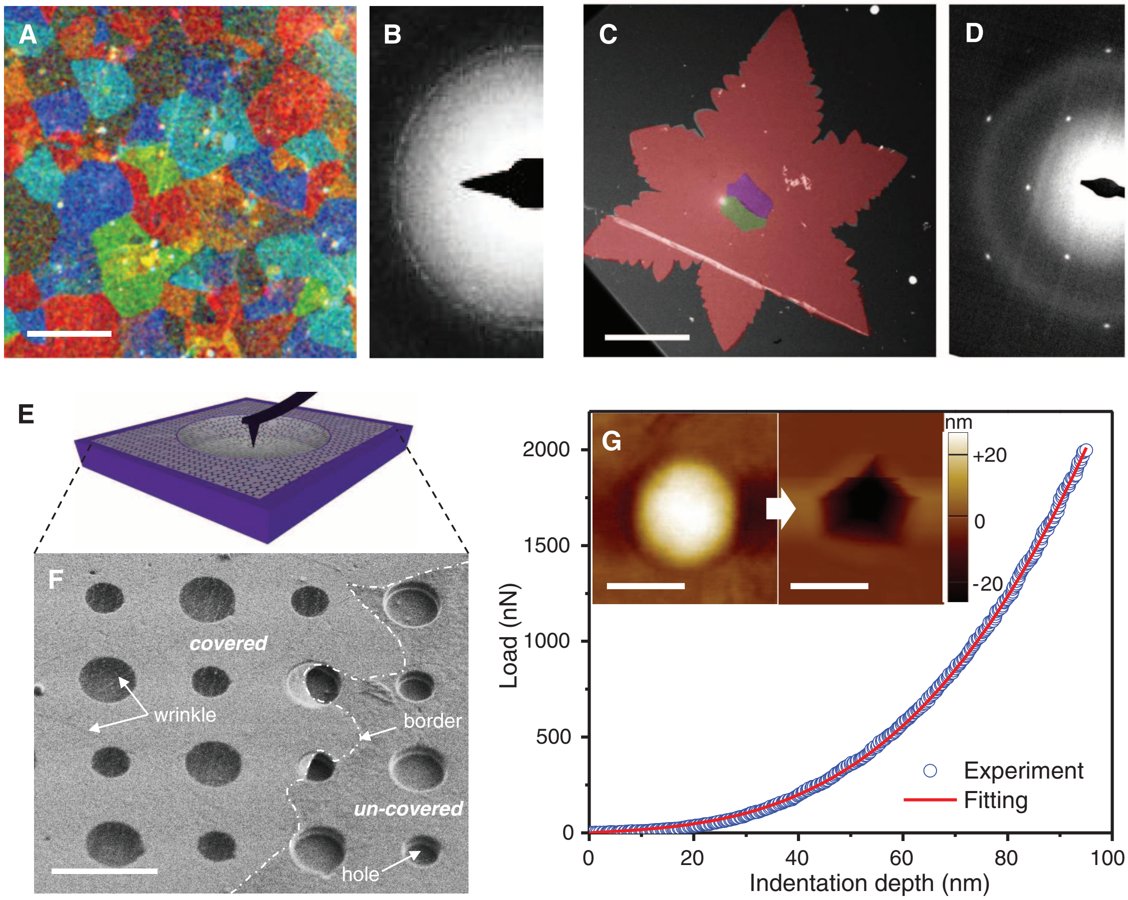

Fig. 1. Materials and testing methods. (**A** and **C**) False-color DF-TEM images and (**B** and **D**) SAED patterns of SG graphene and LG graphene films. (**E**) Schematic of the suspended graphene film over hole for AFM nanoindentation tests. (**F**) SEM images of the suspended LG graphene film over holes. The border of the graphene-covered area is indicated by a dashed line for visualization. Wrinkles often present in the transferred graphene can be seen. (**G**) Force-displacement curve of the SG graphene film in AFM nanoindentation. The red line is a fitting curve to equation 2 of (*1*). (Inset) The AFM topology images of the suspended SG graphene film before and after fracture. Scale bars, (A) and (F) 3 μm; (C) 20 μm; (G) 1 μm.

through scalable methods—such as chemical vapor deposition (CVD)—produces graphene with various defects, especially grain boundaries (*3*–*7*). It is of fundamental importance to understand how the nature and presence of such defects will degrade the mechanical properties. Recent theoretical studies have argued that graphene grain boundaries can be as strong as the pristine lattice, depending on their exact configuration, such as tilt angle (*8*) and arrangement of defects (*9*). On the other hand, nanoindentation tests have shown that both the elastic stiffness and fracture strength of CVD-graphene with micrometer-scale grain size are much smaller than those of defect-free pristine graphene and that fracture occurs at grain boundaries (*3*, *5*). However, continued progress in development of techniques for processing graphene motivates reexamination of this question from an experimental standpoint. Indeed, we find here that techniques used in earlier studies, which were standard practice at the time and remain widely used, significantly degrade the strength of graphene (supplementary materials). In this work, we used new processing techniques that leave graphene's strength intact. We used a commercial nanoindenter to test a large number of samples for statistical analysis and combined nanoindentation and transmission electron microscopy (TEM) characterization to test individual grain boundaries. The data were analyzed by using a multiscale model that is based on density functional theory and has been experimentally validated for pristine graphene.

Two types of graphene were grown on copper foil: continuous graphene films with small grains (SG) and isolated single-crystals with large grains (LG) (supplementary materials, materials and methods). Dark-field TEM (DF-TEM) imaging (*3*) was used to map the grain structure of the graphene films (Fig. 1, A and C); each false-color area indicates a distinct crystal orientation from the selected area electron diffraction (SAED) patterns of Fig. 1, B and D. These patterns confirm that the SG graphene is similar to the films studied previously (*3*–*5*): It is polycrystalline, with 1- to ~5-μm grains that are stitched at well-defined grain boundaries, that have been observed to consist of pentagon and heptagon carbon rings without any other defects, such as holes (*3*, *4*). Small bilayer patches are occasionally present in the middle of grains. The star-shaped LG graphene grains are 50- to ~200-μm single crystals (Fig. 1D) (*10*, *11*) of single-layer graphene with small multilayer patches at the center. All of the nanoindentation experiments reported below were performed on the single-layer areas of the SG and LG graphene films.

To create suspended membranes, graphene films grown on copper foil were transferred onto a silicon dioxide substrate with an array of holes with 1- and 1.5-μm diameters (Fig. 1E; figs. S1 and S2; and supplementary materials, materials and methods). We found that two of the processing techniques used in previous studies (*3*, *5*) severely weakened the grain boundaries in CVD-graphene: etching the copper with ferric chloride ($FeCl_3$) and removal of a polymer support by baking in air (figs. S3 and S4). Both steps were avoided herein; the copper was etched with ammonium persulfate instead of $FeCl_3$, and polydimethylsiloxane (PDMS) was used to support the graphene during copper etching and to dry-stamp it onto the substrate without baking. The transferred LG graphene film is shown in the scanning electron microscopy (SEM) image of Fig. 1F (SG graphene is shown in fig. S3A). The graphene films form membranes tautly suspended above the holes, with little contamination. Raman spectroscopy confirms that the membranes are highly crystalline graphene with few defects (fig. S5).

We used nanoindentation to measure mechanical properties of the suspended membranes, as described in (*2*, *12*). A representative force-displacement curve obtained by using an AFM with a diamond tip of 26-nm radius is shown in Fig. 1G. The curve was well fitted by use of a quasi-empirical polynomial form (*2*). The cubic fitting parameter yielded 99% confidence intervals for the mean of elastic stiffness of 328 ± 15 N/m near that of pristine graphene (340 N/m) and an order of magnitude higher than the value previously reported for CVD-graphene (55 N/m) (*5*). Moreover, the force required to break the membrane is 2000 ± 420 nN, which is much greater than that previously observed (50 to 120 nN) (*3*, *5*). A SG membrane before and after fracture are shown in the AFM images in the inset. The samples showed no sign of slippage at the periphery, and the fracture pattern was similar to that observed for pristine graphene (fig. S6).

For statistical analysis of stiffness and strength, we tested a large number of specimens using a nanoindenter, with a 38-nm-radius diamond tip (fig. S7A). Each membrane was cyclically tested to increasing depth to fracture; the nonhysteretic force-displacement curves were analyzed as above. Histograms of the derived elastic stiffness are shown in Fig. 2, A and B, for LG and SG graphene (that of pristine graphene is available in fig. S7B). We obtained elastic moduli of 324 ± 13, 339 ± 17, and 328 ± 17 N/m (which correspond to a 3D Young's modulus of ~1 TPa) for pristine, LG, and SG graphene, respectively. According to one-way analysis of variance (ANOVA) analyses, there are no statistical differences among these three values or between these and the value previously obtained for pristine graphene (fig. S8A and table S1) (*2*); all are in agreement with theoretical predictions in the absence of grain boundaries (*13*). The wider distributions observed for SG and LG graphene may be due to the presence of wrinkles and small bilayer patches in the CVD-grown membranes.

The measured fracture loads for LG and SG membranes are shown in Fig. 2, C and D (pristine is available in fig. S7C). The measurements yield fracture loads of 3410 ± 260, 3370 ± 340, and 2590 ± 380 nN for the pristine, LG, and SG films, respectively. The fracture load of the SG films is statistically different from that of the pristine and

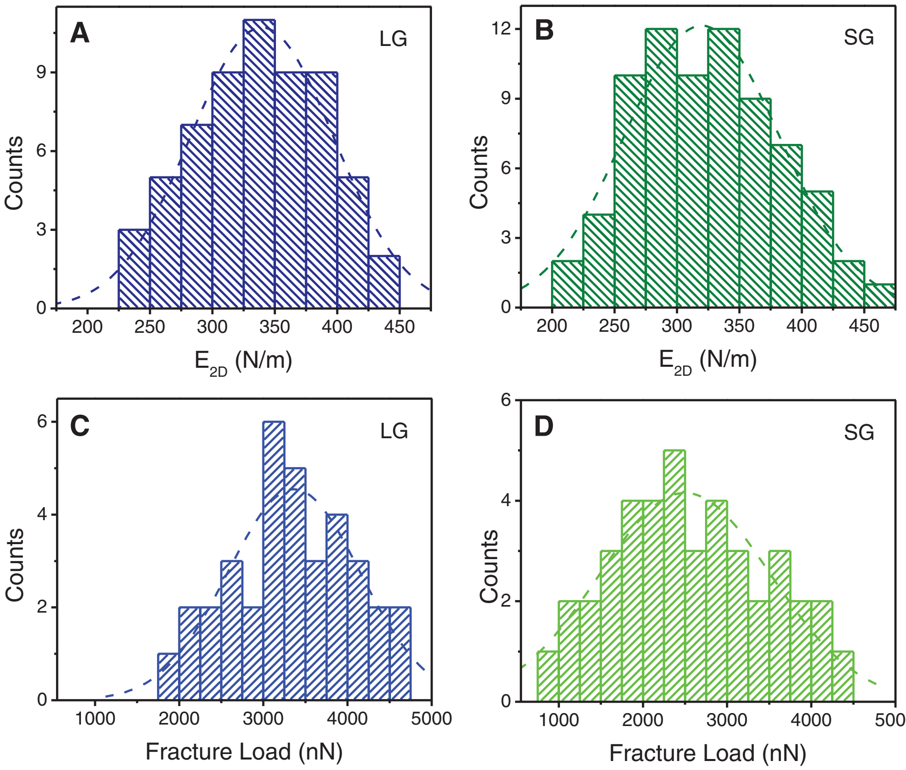

Fig. 2. Statistical analyses of nanoindenter results. (**A** and **B**) The histograms of the elastic stiffness of (A) LG and (B) SG graphene films. (**C** and **D**) The histograms of fracture load for (C) LG and (D) SG graphene films. A tip with a 38-nm radius was used in all tests. The dashed lines indicate fitted Gaussian distributions.

LG films, whereas there is no statistical difference between the fracture loads of the pristine and LG graphene according to one-way ANOVA (fig. S8B and table S2). The smaller mean fracture load and wider distribution observed for SG graphene indicates that the strength is influenced by the randomly occurring defects and grain boundaries in the membranes. Nevertheless, the measured fracture load of the SG graphene is much larger than seen in previous measurements (*3*, *5*).

We calculated the breaking strength of the graphene films as a function of the measured fracture load and tip diameter with an experimentally validated multiscale model based on atomic-scale ab initio density functional theory (*14*). This constitutive model informs a continuum description of anisotropic and nonlinear elastic behavior for in-plane deformation (*14*, *15*) that permits numerical modeling of the stress in the graphene up to the point of rupture. Shown in fig. S9 is the equibiaxial true stress versus load under the center of a 38-nm indenter tip for pristine graphene, which yields an equibiaxial breaking strength of 34.5 N/m (103 GPa, when expressed as a 3D value). The mechanical strength or peak stress that can be supported by graphene is a function of the loading configuration. For uniaxial stress in the armchair direction, the same model predicts a strength of 39.5 N/m (118 GPa), which is consistent with our previously reported value of 42 ± 4 N/m for the same loading configuration (supplementary materials). With an identical fracture load, LG graphene has an equivalent breaking strength to pristine graphene. The average equibiaxial strength of SG graphene is only slightly smaller, 33 N/m (98.5 GPa). A similar value was obtained for SG membranes tested with AFM. These results demonstrate that polycrystalline graphene with well-stitched grains can act as a large-area ultrastrong material.

Because the stress decreases inversely with distance from the indenter tip, the stress under the tip at rupture does not necessarily correspond to the grain boundary strength. Therefore, we performed indentation tests directly on a few grain boundaries identified through TEM. SG films were transferred onto TEM grids with 2.5-μm holes by using a poly(methyl methacrylate) (PMMA) transfer technique (*3*, *7*), followed by annealing in hydrogen and argon so as to remove the PMMA without reducing the strength of the films. The bright-field TEM (BF-TEM) image of Fig. 3A shows a suspended SG film, with adsorbates (likely PMMA residue) that decorate grain boundaries, as confirmed with higher-resolution imaging (Fig. 3B) (*3*, *13*); these adsorbates are not observed in LG films (fig. S10). The corresponding grain structure is illustrated in the DF-TEM map of Fig. 3C. The adsorbates render the grain boundaries visible in AFM (Fig. 3E and fig. S11) but are also present at wrinkles, so that AFM imaging alone is not sufficient to identify grain boundaries. Adsorbates are not expected to affect the grain

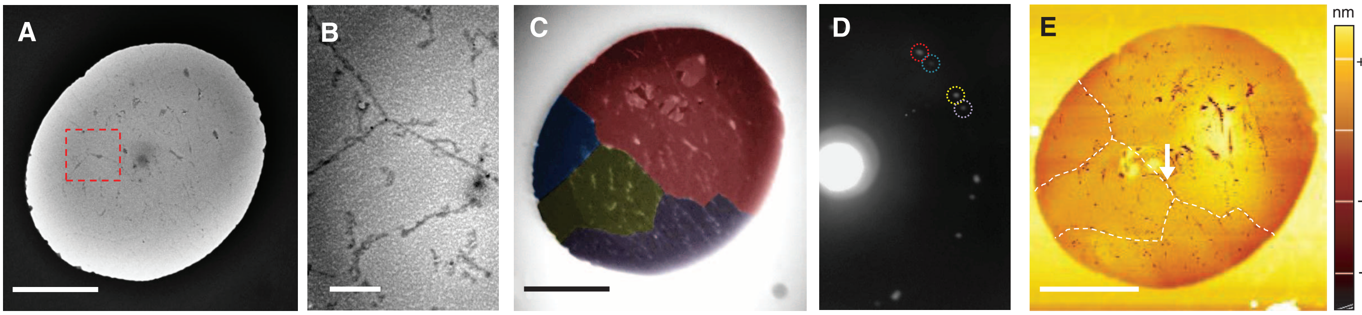

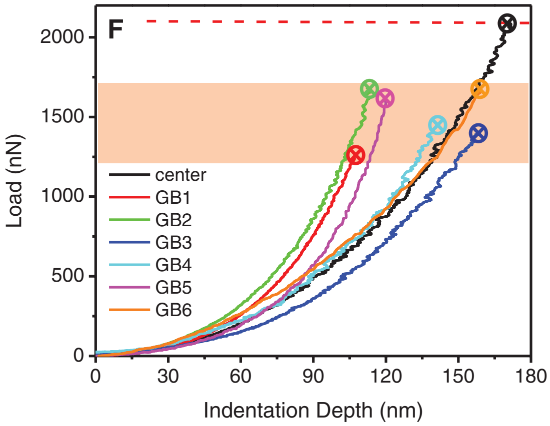

Fig. 3. TEM observation of grain boundaries and AFM nanoindentation on grain boundaries. (**A** and **B**) BF-TEM images of (A) suspended SG graphene film over a hole and (B) enlarged BF-TEM image of red-dashed area in (A). (**C**) False-color DF-TEM image. (**D**) SAED of the same region. The diffraction spots corresponding to each color of (C) are indicated in (D) with circles of different colors. (**E**) AFM topology image shows that arrays of PMMA residue adhere to grain boundaries. The grain boundaries and indentation point are indicated by dashed lines and the white arrow. (**F**) AFM indentation results show that fracture occurs at a slightly lower load when AFM tip indents on the grain boundary. Scale bars, 1 μm; (B) 200 nm.

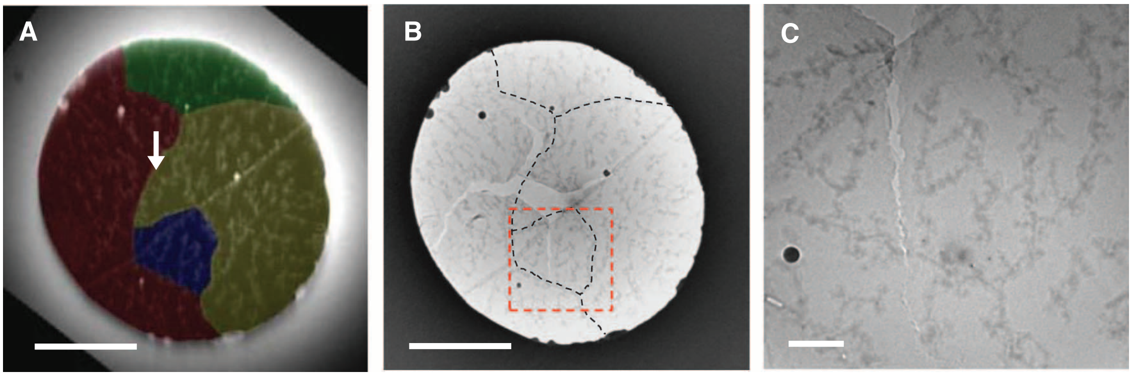

Fig. 4. Crack propagation during nanoindentation. (**A**) False-color DF-TEM image of the suspended SG graphene film over a hole before indentation. The white arrow indicates the indentation point. (**B**) BF-TEM image after indentation. The black-dashed lines indicate grain boundaries. (**C**) Enlarged BF-TEM image of the red-dashed area of (B). Scale bars, 1 μm; (C) 200 nm.

boundary properties because of the very low stiffness and strength of PMMA.

The results of six indentation tests are shown in Fig. 3F, with the tip placed directly on asymmetric tilt grain boundaries near the center of the membrane. An additional test performed at the center of a grain away from grain boundaries (fig. S11I) yielded fracture load similar to that of pristine graphene. The fracture loads at the grain boundaries are 20 to 40% smaller but still an order of magnitude larger than previously measured (*3*, *5*). The same multiscale analysis described above gives a range of equibiaxial stress of 30 to 33 N/m (90 to 99 GPa) for the strength of the grain boundaries, representing at most a 15% reduction from the intrinsic strength. These results confirm that grain boundaries in graphene can achieve ultrahigh strength.

Atomistic scale simulations of symmetric tilt grain boundaries predict that grain boundaries with large tilt angles can achieve near-intrinsic strength (above 30 N/m), but those with low tilt angles possess a lower strength of 13 to 26 N/m, depending on the precise arrangement of defects (*8*, *9*). The simulated grain boundaries consist of periodically spaced pentagon-heptagon ring defects along straight grain boundaries. The simulations predict rupture initiation at the bond joining the pentagonal and heptagonal (5-7) rings, and that decreasing its initial equilibrium length (smaller misfit "prestrain") increases grain boundary strength (*8*, *9*).

The asymmetric tilt grain boundaries in the experiments, which cover a wide range of tilt angles (fig. S12 and table S3), consistently exhibited strength above 30 N/m, suggesting that the predicted variation in strength with tilt angle does not occur in these samples. The tortuous atomic structure of random (*3*) asymmetric grain boundaries is substantially more complex than that assumed for the simulations of symmetric grain boundaries (*8*, *9*). The more complex energy-minimizing structure (*16*) likely leads to a smaller misfit "prestrain" of the critical atomic bonds at in the 5-7 defects, thus explaining the ultrahigh strength (details are available in the supplementary materials) (fig. S12 and table S3).

In addition to well-stitched grain boundaries, we also occasionally observed boundaries in which the adjacent graphene grains overlap (50 nm in width) but do not covalently join (*3*, *4*) (fig. S13). These boundaries were observed to be extremely weak, with no measurable force upon AFM indentation. Overlapped grain boundaries have been observed to possess higher conductance (*4*) than that of stitched boundaries but will result in much weaker films.

To further elucidate the fracture behavior of graphene, AFM nanoindentation on SG membranes was performed to failure, and the ruptured films were observed with TEM. Indentation on a grain boundary (Fig. 4A, white arrow) initiates an intergranular crack (Fig. 4B and fig. S14) under the approximately equibiaxial stress state beneath the indenter tip, thus demonstrating the grain boundary to be somewhat weaker than graphene. The crack later kinks into the adjoining grains because of the more complex stress state. Contrary to the prediction or experimental observation during electron irradiation (*13*), the torn edges of the transgranular cracks have irregular saw-tooth shapes, as shown in the enlarged BF-TEM image of Fig. 4C and fig. S15.

Our measurements reveal that the elastic stiffness and strength of CVD-graphene are comparable with those of pristine graphene, despite the existence of grain boundaries. Moreover, the strength of grain boundaries is much stronger than previously measured, which is in agreement with the maximum values predicted in simulations. This study establishes CVD-graphene as a large-area, high-strength material for flexible electronics and strengthening components.

References and Notes

1. M. Meyers, K. Chawla, *Mechanical Behavior of Materials* (Cambridge, London, ed. 2, 2009).
2. C. Lee, X. D. Wei, J. W. Kysar, J. Hone, *Science* **321**, 385 (2008).
3. P. Y. Huang *et al.*, *Nature* **469**, 389 (2011).
4. A. W. Tsen *et al.*, *Science* **336**, 1143 (2012).
5. C. S. Ruiz-Vargas *et al.*, *Nano Lett.* **11**, 2259 (2011).
6. Q. K. Yu *et al.*, *Nat. Mater.* **10**, 443 (2011).
7. K. Kim *et al.*, *ACS Nano* **5**, 2142 (2011).
8. R. Grantab, V. B. Shenoy, R. S. Ruoff, *Science* **330**, 946 (2010).
9. Y. Wei *et al.*, *Nat. Mater.* **11**, 759 (2012).
10. X. S. Li *et al.*, *J. Am. Chem. Soc.* **133**, 2816 (2011).
11. N. Petrone *et al.*, *Nano Lett.* **12**, 2751 (2012).
12. M. Poot, H. S. J. van der Zant, *Appl. Phys. Lett.* **92**, 063111 (2008).
13. K. Kim *et al.*, *Nano Lett.* **12**, 293 (2012).
14. X. D. Wei, J. W. Kysar, *Int. J. Solids Struct.* **49**, 3201 (2012).
15. X. D. Wei, B. Fragneaud, C. A. Marianetti, J. W. Kysar, *Phys. Rev. B* **80**, 205407 (2009).
16. F. Ernst *et al.*, *Z. Metallk.* **87**, 911 (1996).

Acknowledgments: We acknowledge support from Air Force Office of Scientific Research grants FA9550-09-1-0048 and FA9550-09-1-0705 and NSF grant CMMI-0927891. C.L. was supported by Basic Science Research Program (2011-0014209) and the Global Frontier Research Center for Advanced Soft Electronics (2011-0031629) through the National Research Foundation funded by the Korean government Ministry of Education, Science, and Technology. We thank P. Y. Huang and D. Muller (Cornell University) for help in TEM imaging.

Supplementary Materials

www.sciencemag.org/cgi/content/full/340/6136/1073/DC1
Materials and Methods
Supplementary Text
Figs. S1 to S15
Tables S1 to S3
References (*17*–*31*)

14 January 2013; accepted 16 April 2013
10.1126/science.1235126

Unwinding of a Skyrmion Lattice by Magnetic Monopoles

P. Milde,[1]* D. Köhler,[1] J. Seidel,[2] L. M. Eng,[1] A. Bauer,[3] A. Chacon,[3] J. Kindervater,[3] S. Mühlbauer,[4] C. Pfleiderer,[3] S. Buhrandt,[5] C. Schütte,[5] A. Rosch[5]

Skyrmion crystals are regular arrangements of magnetic whirls that exist in a wide range of chiral magnets. Because of their topology, they cannot be created or destroyed by smooth rearrangements of the direction of the local magnetization. Using magnetic force microscopy, we tracked the destruction of the skyrmion lattice on the surface of a bulk crystal of $Fe_{1-x}Co_xSi$ ($x = 0.5$). Our study revealed that skyrmions vanish by a coalescence, forming elongated structures. Numerical simulations showed that changes of topology are controlled by singular magnetic point defects. They can be viewed as quantized magnetic monopoles and antimonopoles, which provide sources and sinks of one flux quantum of emergent magnetic flux, respectively.

The notion of topological stability refers to those properties of a system that remain unchanged under continuous (elastic) deformations such as bending or stretching (*1*, *2*). Because topologically stable structures cannot easily be created and destroyed, they play an important role in both fundamental and applied physics. An area in which topological stability is important are spin configurations in magnetic materials. Magnetic domain walls are examples of planar, two-dimensional topological defects. Various types of magnetic whirls form one-dimensional topological structures, and hedgehogs, where the magnetization points in all directions, are examples of pointlike (zero-dimensional) defects. A major challenge in systems exhibiting topological stability is to experimentally observe the unwinding of topologically stable configurations and to identify its mechanism.

The recent discovery of skyrmion lattices in chiral magnets with B20 crystal structure (Fig. 1A) has attracted great interest, as it provides an example of lattice order composed of topologically

---

[1] Institut für Angewandte Photophysik, TU Dresden, D-01069 Dresden, Germany. [2] School of Materials Science and Engineering, University of New South Wales, Sydney NSW 2052, Australia. [3] Physik-Department E21, Technische Universität München, D-85748 Garching, Germany. [4] Forschungsneutronenquelle Heinz Maier-Leibnitz, Technische Universität München D-85747 Garching, Germany. [5] Institut für Theoretische Physik, Universität zu Köln, D-50937 Cologne, Germany.

*Corresponding author. E-mail: peter.milde@iapp.de